

See discussions, stats, and author profiles for this publication at: <https://www.researchgate.net/publication/277627119>

Comparison between novel waverider generated from flow past a pointed von Karman ogive and conventional cone-derived waverider

Article in *Proceedings of the Institution of Mechanical Engineers Part G Journal of Aerospace Engineering* · April 2015

DOI: 10.1177/0954410015581404

CITATIONS

20

READS

3,648

4 authors, including:



Feng Ding

National University of Defense Technology

28 PUBLICATIONS 375 CITATIONS

[SEE PROFILE](#)



Wei Huang

National University of Defense Technology

208 PUBLICATIONS 6,206 CITATIONS

[SEE PROFILE](#)

Some of the authors of this publication are also working on these related projects:



Aircraft design, drag reduction and thermal protection for high-speed vehicles [View project](#)



Intelligent control on the shock wave/turbulence boundary layer interaction [View project](#)

Comparison between novel waverider generated from flow past a pointed von Karman ogive and conventional cone-derived waverider

Proc IMechE Part G:
J Aerospace Engineering
2015, Vol. 229(14) 2620–2633
© IMechE 2015
Reprints and permissions:
sagepub.co.uk/journalsPermissions.nav
DOI: 10.1177/0954410015581404
uk.sagepub.com/jaero



Feng Ding^{1,2}, Chi-bing Shen^{1,2}, Jun Liu^{1,2} and Wei Huang^{1,2}

Abstract

This study conducts a comparison between a novel waverider generated from axisymmetric supersonic flow past a pointed von Karman ogive and a conventional cone-derived waverider generated from the axisymmetric supersonic flow past a cone. First, a pointed von Karman ogive is obtained by sharpening the blunt nose of the original von Karman ogive to a point. Then, a cone with the same shock wave radius at the base plane as that of the pointed von Karman ogive when it travels at a designated supersonic speed is designed. Both axisymmetric supersonic flows past the pointed von Karman ogive and the cone are calculated using the method of characteristics, and the two calculated flow fields are employed as the new and conventional basic flow fields of the waveriders, respectively. Second, a novel waverider is generated from the new basic flow field past the pointed von Karman ogive, using the streamline tracing technique, and a conventional cone-derived waverider is generated from the conventional basic flow field past the cone, using the streamline tracing technique. Finally, numerical methods are employed to verify the design procedures of the novel and conventional cone-derived waveriders, and to analyze the differences between both types of waverider. The obtained results show that the novel waverider possesses lower drag and higher lift-to-drag ratios, while the conventional cone-derived waverider has a higher internal volume and volumetric efficiency.

Keywords

Hypersonic vehicle, waverider, von Karman ogive, method of characteristics

Date received: 17 August 2014; accepted: 15 March 2015

Introduction

The achievement of lower drag and a higher lift-to-drag ratio for hypersonic waverider vehicles is the goal of many researchers in the field of aerodynamic design. A waverider is any supersonic or hypersonic lifting body that is characterized by an attached, or nearly attached, bow shock wave along its leading edge.¹ Past research has widened the waverider design space by attempting to establish a range of basic flow field choices from which the waverider can be generated. Specifically, Nonweiler,² Jones,³ Rasmussen,⁴ Corda,^{5,6} and He⁷ have employed flows past a wedge, circular cone, elliptic cone, power-law body^{8,9} and curved cone at a zero angle of attack, respectively, as basic flow fields for the generation of waveriders. Further, Goonko¹⁰ and Mazhul¹¹ have used the convergent flow inside constricting ducts and an isentropic compression flow, respectively, as basic flow fields for waverider generation. All the above-listed flows can be classified as axisymmetric flows. In contrast, Takashima¹² derived a non-axisymmetric flow field from flow past a wedge-cone

body, and used it as the basic flow field for the generation of waveriders.

The von Karman ogive¹³ is one of the minimum-drag bodies of revolution at a zero angle of attack at supersonic speeds. It is often used as the nose cone in the aerodynamic design of a rocket or missile. Therefore, one might intuitively speculate that the waverider generated from the flow past a von Karman ogive may have a lower drag and higher lift-to-drag ratio when compared with the waverider generated by the flow past a cone. However, to the best of the authors' knowledge, comparisons between

¹College of Aerospace Science and Engineering, National University of Defense Technology, Changsha, Hunan, People's Republic of China

²Science and Technology on Scramjet Laboratory, National University of Defense Technology, Changsha, Hunan, People's Republic of China

Corresponding author:

Chi-bing Shen, College of Aerospace Science and Engineering, National University of Defense Technology, Changsha, Hunan 410073, People's Republic of China.

Email: cbshen@nudt.edu.cn

the two types of waveriders have rarely been reported in the literature. Therefore, in this study, a comparison between waveriders generated from flows past a pointed von Karman ogive and past a cone is conducted. First, the basic flow fields for the pointed von Karman ogive and cone waveriders are designed and generated, and then numerical methods are used to verify the design procedures and to draw comparisons between the characteristics of both waveriders. The resultant drag and lift-to-drag ratios are determined.

Design and generation of basic flow fields

Von Karman used the slender-body theory to obtain the minimum-drag ogive for a given object length, L , and base radius, R , moving at supersonic speeds; this is referred to as the von Karman ogive.¹³ However, the von Karman ogive is a blunt body and when it travels at a supersonic or hypersonic speed, the blunt nose will induce a detached shock wave and a subsonic flow field will form in the region surrounding the tip of the body. In order to ensure the creation of a completely supersonic flow with an attached shock wave when the ogive travels at a supersonic speed, a von Karman ogive with a pointed nose (hereafter simply called the ‘pointed von Karman ogive’) is required.

A pointed von Karman ogive is obtained by pointing, or sharpening, the blunt nose of the von Karman ogive. As shown in Figure 1, the blunt nose contour, OA , of the original von Karman ogive is replaced with a straight cone contour, O_1A , at point A , and the angle of the slope at A is θ_A . The contour, O_1AH , is the contour of the pointed von Karman ogive. In Figure 2, the shape of a cone and of a pointed von Karman ogive, and their corresponding attached shock waves when they travel at a designated supersonic speed are illustrated. In order to ensure that the trailing-edge curves of the novel and conventional waverider free-stream surfaces remain identical, the radii (R_s in Figure 2) of both shock waves at the base planes of the cone and the pointed von Karman ogive must be identical. This is the fundamental constraint for both basic flow fields in the present study. Given the parameters L , R , and θ_A , the pointed von Karman ogive can be determined. Then, a corresponding cone that can adhere to the fundamental constraint is solved. The specific parameters of

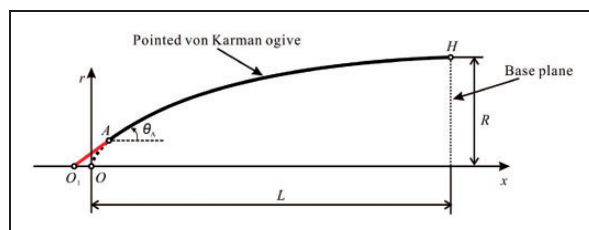


Figure 1. Schematic illustration of pointed von Karman ogive.

this cone and the pointed von Karman ogive, as well as the properties of the free-stream flow, are listed in Table 1.

Next, two axisymmetric supersonic flows past the cone and the pointed von Karman ogive are calculated using the method of characteristics (MOC),¹⁴ which affords accuracy and speed in calculation.¹⁵ The obtained flow field past the pointed von Karman ogive is employed as the new basic flow field of the waverider, and the obtained flow field past the cone is employed as the conventional waverider basic flow field.

Physical model and numerical method

Physical model

As illustrated in Figure 3(a), a waverider is composed of three surfaces: the free-stream surface, compression-stream surface, and base surface. The compression-stream surface is obtained by lofting a group of streamlines. The curve where the free-stream surface intersects the shock wave is called the leading-edge curve, while the curve where the base surface intersects the free-stream or compression-stream surface is called the trailing-edge curve.

In this study, the novel waverider generated from the new basic flow field past the pointed von Karman ogive is termed the von Karman waverider.

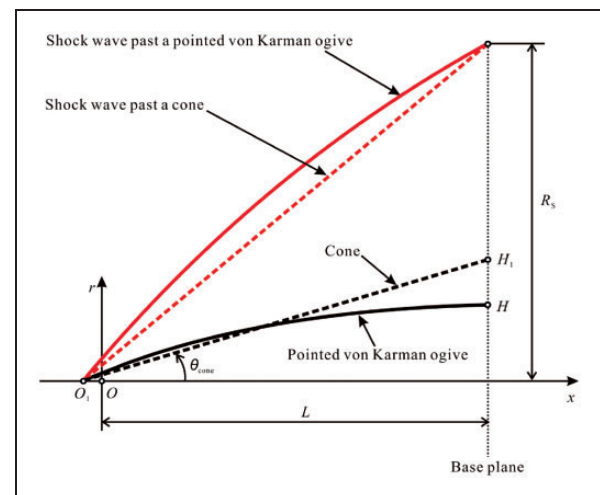


Figure 2. Schematic illustration of two axisymmetric supersonic basic flow fields past cone and pointed von Karman ogive.

Table 1. Specific parameters of cone, pointed von Karman ogive, and free-stream flow properties.

M_0	P_0 (Pa)	T_0 (K)	L (m)	R (m)	θ_A (°)	θ_{cone} (°)
6	2511.1	221.64	10.0	1.6	19.0	12.4288
	8	9				68

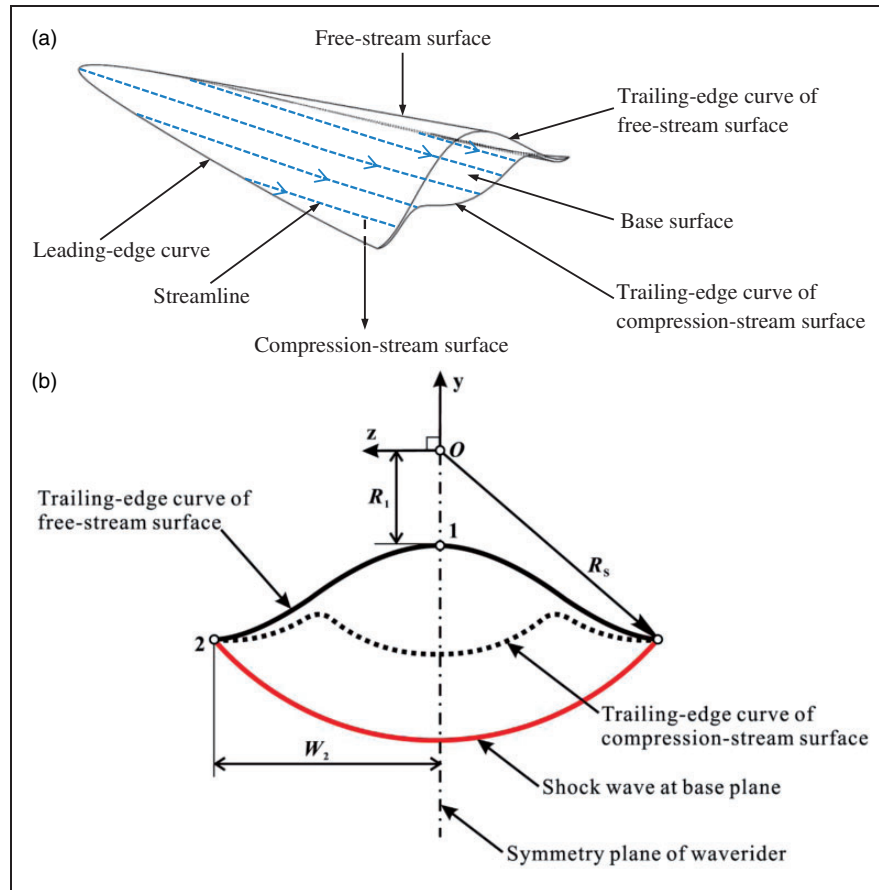


Figure 3. Properties of a waverider. (a) Isometric view and (b) rear view (illustration of trailing-edge curve).

The conventional waverider generated from the conventional basic flow field past the cone is usually termed a cone-derived waverider.¹⁶ The trailing-edge curve of the free-stream surface for the two waveriders is described by a fourth-order polynomial curve, and its function is expressed by equation (1) in the Cartesian coordinate system shown in Figure 3(b). As shown in Figure 3(b), choosing the boundary condition that the slope at the endpoint 2 is zero, and given the parameters R_1 and W_2 , the coefficients, i.e., a , b , and c in equation (1) can be determined by equations (2) to (4).

In the present study, the parameters $R_1 = 0.2R_S$ and $W_2 = 0.8R_S$. R_S is the radius of the shock wave at the base plane (see Figures 2 and 3b). When the basic flow field is calculated using the MOC, the value of R_S can be determined. And then the geometric models for the two waveriders are generated, as shown in Figure 4.

$$y = a + bz^2 + cz^4, \quad z \geq 0 \quad (1)$$

$$a = -R_1 \quad (2)$$

$$b = \frac{2(R_1 - \sqrt{R_S^2 - W_2^2})}{W_2^2} \quad (3)$$

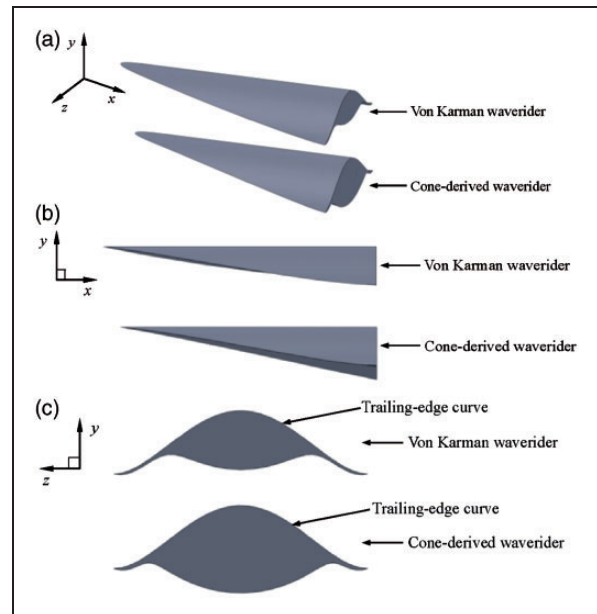


Figure 4. Comparison of geometric models between cone-derived and von Karman waveriders. (a) Isometric view, (b) side view, and (c) rear view.

$$c = \frac{\sqrt{R_S^2 - W_2^2} - R_1}{W_2^4} \quad (4)$$

Table 2. Structured grid independency analysis employed in von Karman waverider ($H = 25$ km, $M_0 = 6.0$, $\alpha = 0^\circ$).

	Number of cells	C_L	C_D	C_{M_Z}	ΔC_L	ΔC_D	ΔC_{M_Z}
Coarse grid	1,342,335	0.502959	0.116346	-0.003022	0.002%	1.75%	0.60%
Medium grid	1,933,835	0.502410	0.116152	-0.003069	-0.11%	1.58%	2.16%
Refined grid	2,525,335	0.502947	0.114342	-0.003004	-	-	-

Table 3. Structured grid independency analysis employed in cone-derived waverider ($H = 25$ km, $M_0 = 6.0$, $\alpha = 0^\circ$).

	Number of cells	C_L	C_D	C_{M_Z}	ΔC_L	ΔC_D	ΔC_{M_Z}
Coarse grid	1,426,617	1.006481	0.280341	-0.137640	-0.46%	1.97%	0.002%
Medium grid	2,039,257	1.007474	0.280290	-0.137872	-0.36%	1.95%	0.17%
Refined grid	2,651,897	1.011133	0.274921	-0.137636	-	-	-

Numerical method

The three-dimensional coupled implicit Reynolds-averaged Navier–Stokes (RANS) equations and the two-equation shear-stress transport (SST) $k-\omega$ turbulence model have been employed to numerically simulate the viscous flow fields and viscous aerodynamic performances of the two waveriders using the commercial software program ANSYS Fluent.¹⁷ Specifically, the second-order spatially accurate upwind scheme that applies the advection upstream splitting method (AUSM) to the flux vector is utilized, the Green-Gauss cell-based gradient method is used to compute the gradients, and the Courant-Friedrichs-Levy (CFL) number is maintained at 0.5 by using proper under-relaxation factors to ensure stability.¹⁸ The enhanced wall treatment¹⁷ is introduced into the flow in the near-wall region in the selected model, and no-slip velocity boundary condition is imposed along the walls of the model.¹⁹ The thermal boundary condition at the walls is considered to be adiabatic in this article.²⁰ The pressure far field is as the boundary condition of the inflow and outflow field. The air is assumed to be a thermally and calorically perfect gas²¹ with the viscosity modelled according to the well-known Sutherland law,²² which is expressed by equation (5).²³ The thermal conductivity of the gas is determined by the Prandtl number, and it is expressed by equation (6).²⁴ The specific heat ratio, γ , is also assumed to be a constant value, namely 1.4 considered in this article.²⁵

$$\mu = 1.458 \times 10^{-6} \frac{T^{1.5}}{T + 110.4} \quad (5)$$

$$k = \frac{\mu C_p}{Pr} \quad (6)$$

where μ is the dynamic viscosity coefficient; T is the static temperature of the air, and it is given in Kelvin;

k is the thermal conductivity of the gas, C_p is the specific heat at constant pressure, and Pr is the Prandtl number.

The solutions can be considered to converge if the residuals reach their minimum values after falling by more than four orders of magnitude, and the difference between the computed inflow and outflow mass flux falls below 0.1%.

Because of the symmetry of the geometric configurations, only half of the flow field is required to perform the numerical simulation of the two waveriders. Three structured grid scales for the two waveriders are used to analyze the grid independency in the numerical process, namely coarse, medium, and refined grids. To ensure accuracy in the solution of the turbulence flow, a value of y^+ (the dimensionless wall distance, and can be defined by equation (7)) less than 1 is used for the main portion of the wall flow region. The detailed information for the grid independency analysis employed in the two waveriders at the flight Mach number of 6.0 and a cruising height of 25 km with a 0° angle of attack is illustrated in Tables 2 and 3. In Tables 2 and 3, the variation percentages of the lift, drag, and pitching moment coefficients for the coarse and medium grids are estimated relative to the refined grid. From Tables 2 and 3, the grid scale makes only a slight difference and verifies the grid independency. To reduce the computational time, the medium grid scale is used for the following investigations for the two waveriders, and the medium structured grid employed in the von Karman waverider is shown in Figure 5.

$$y^+ = \frac{u_\tau y}{\nu} \quad (7)$$

where y^+ is the dimensionless distance from the wall for a wall-bounded flow, and it is commonly used in defining the law of the wall; u_τ is the friction velocity at the nearest wall; y is the distance to the nearest wall; and ν is the local kinematic viscosity coefficient of the fluid.¹⁷

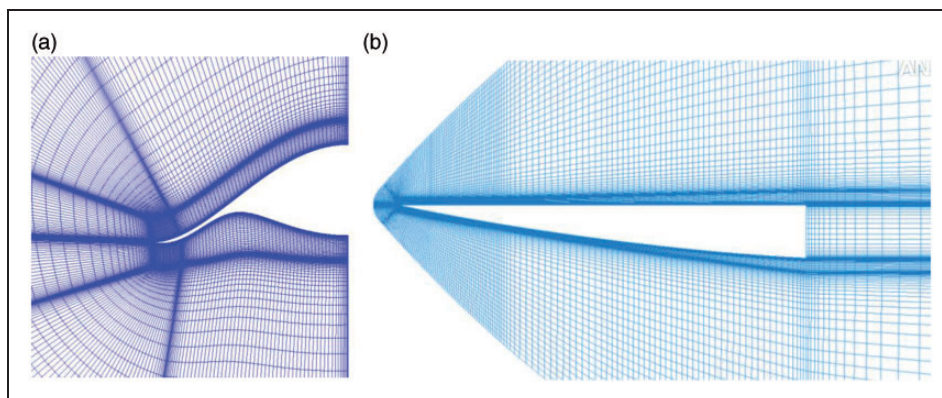


Figure 5. Schematic diagram of medium structured grid employed in von Karman waverider. (a) Grid at the base plane and (b) grid at the symmetry plane.

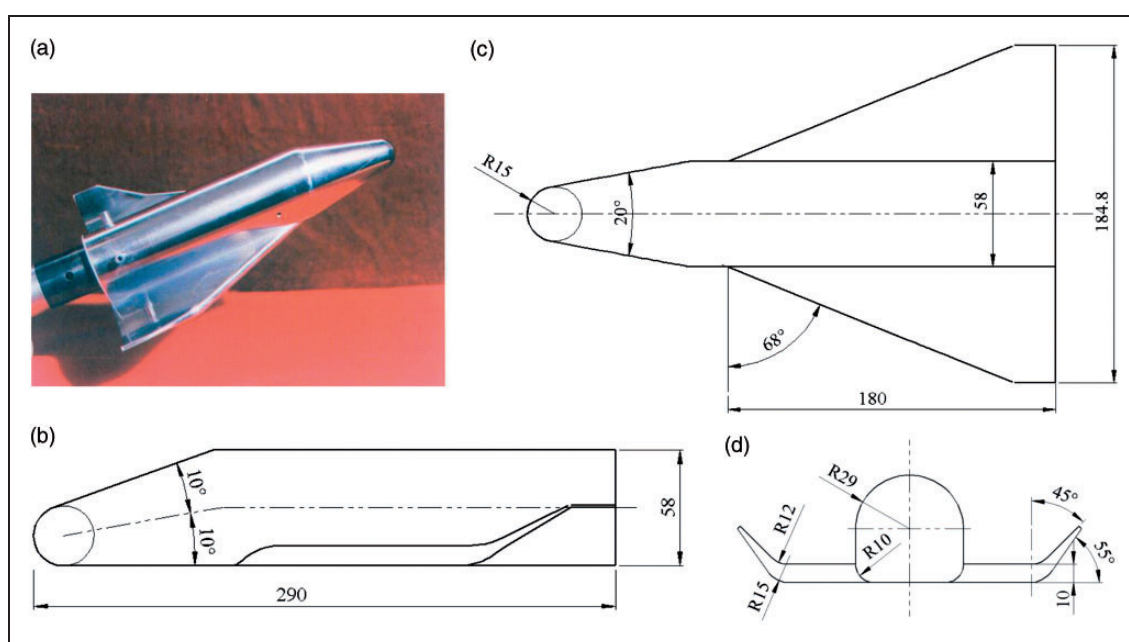


Figure 6. Experimental model and three views of space shuttle used for wind tunnel experiments²⁶ (unit: mm). (a) Experiment model²⁶, (b) side view, (c) top view, and (d) rear view.

The Euler equations are employed to numerically simulate the inviscid flow fields in the same problem formulation by using ANSYS Fluent.¹⁷ Specifically, the Euler equations are solved using the density-based (coupled) implicit solver. The second-order spatially accurate upwind scheme that applies the AUSM method to the flux vector is utilized, and the least-squares cell-based method is used to compute the gradients. The CFL number is set at 0.5. As indicated previously, the air is assumed to be a thermally and calorically perfect gas. Convergence is assumed to be attained in accordance to the same conditions as those described above.

In this study, the design condition is as follows: a flight Mach number of 6.0 and a cruising height of 25 km with a 0° angle of attack. The off-design flight Mach numbers are 4.0 and 8.0, the off-design angles of attack are 2°, 4°, and 6°, while the cruising height

remains at 25 km. At the height of 25 km, the atmosphere parameters are used as the baseline values of the design, where $P_0 = 2511.18$ Pa and $T_0 = 221.649$ K. Moreover, the angle of attack is measured between the free-stream surface and the free-stream direction.

Code validation

In order to investigate the accuracy of the numerical methods employed in this study, two cases, i.e. case 1 and case 2, are chosen to complete the code validation.

Case 1. The experimental model of the space shuttle²⁶ (shown in Figure 6(a)) is the case 1 which is applied to validate the numerical simulations, as done in our previous works.²⁷ The experimental model consisted of three separate pieces: nose, fuselage, and two



Figure 7. FD-14A hypersonic shock wind tunnel.²⁸

wings. Its body length is 290.0 mm, maximum horizontal size is 184.8 mm, and maximum height is 58.0 mm. The detailed dimensions of the experimental model can be seen in Figure 6(b) to (d).

The experiment was carried out in FD-14A hypersonic shock wind tunnel of CARDC (China Aerodynamics Research and Development Center) which is shown in Figure 7. The facility is a conventional reflected shock tube with an attached contoured nozzle in order to expand the high pressure and temperature gas (nitrogen) to hypersonic conditions. The conical contoured nozzle provides a useful jet of 1 m diameter inside the test section.²⁶ Details of this tunnel have been reported by Liu et al.^{24,28} The boundary conditions for the free stream are set as a Mach number of 8.04, a Reynolds number per unit of $1.13 \times 10^7/\text{m}$, a total pressure of 7.8 MPa, and a total temperature of 892 K, in accordance to the experimental setup in Li.²⁶ The detailed aerodynamic performance data of the space shuttle measured during the wind tunnel experiment²⁶ is listed in Table 4. Moreover, in this case, the reference length and area are 29.0 cm and 100.0 cm^2 , respectively. The reference point for the pitching moment coefficient shown in Table 4 is the vertex of the space shuttle.

It is worth noting that the stagnation temperature (temperature near wall, where gas velocity is equal to zero) downstream a normal shock wave is equal to the free-stream total temperature, i.e. 892 K for this space shuttle case. Considering that the stagnation temperature (892 K) is less than 2000 K, the dissociation does not become important for this space shuttle case, due to the fact that the dissociation of O_2 begins when the temperature reaches about 2000 K.²⁹ Thus, the real gas effects is not considered in the validation of numerical simulation. The air is assumed to be a thermally and calorically perfect gas, as described above.

Table 4. Aerodynamic performance data of the space shuttle measured during the wind tunnel experiment.²⁶

M_0	α (°)	C_L	C_D	C_{Mz}	L/D
8.04	−5	−0.1396	0.1447	0.0820	−0.965
8.04	0	−0.0607	0.1120	0.0270	−0.542
8.04	5	0.0067	0.1070	−0.0190	0.063
8.04	10	0.1518	0.1293	−0.1170	1.174
8.04	15	0.3347	0.1901	−0.2600	1.761
8.04	20	0.6060	0.3174	−0.4480	1.909
8.04	25	0.8768	0.5048	−0.6610	1.737
8.04	30	1.1510	0.7604	−0.8860	1.514

Table 5. Structured grid independency analysis employed in space shuttle (case I) for SST $k-\omega$ turbulence model code ($M_0 = 8.04$, $\alpha = 0^\circ$).

	Number of cells	C_D	ΔC_D
Coarse grid	2,904,554	0.126805	−0.54%
Medium grid	3,753,594	0.125981	−1.19%
Refined grid	4,814,894	0.127493	—

In this study, three structured grid scales are introduced to analyze the grid independency. Table 5 presents the structured grid independency analysis obtained from the SST $k-\omega$ turbulence model code at the Mach number of 8.04 and the 0° angle of attack. In Table 5, the variation percentages of the drag coefficients for the coarse and medium grids are estimated relative to the refined grid.

From Table 5, the grid scale makes only a slight difference and verifies the grid independency for the

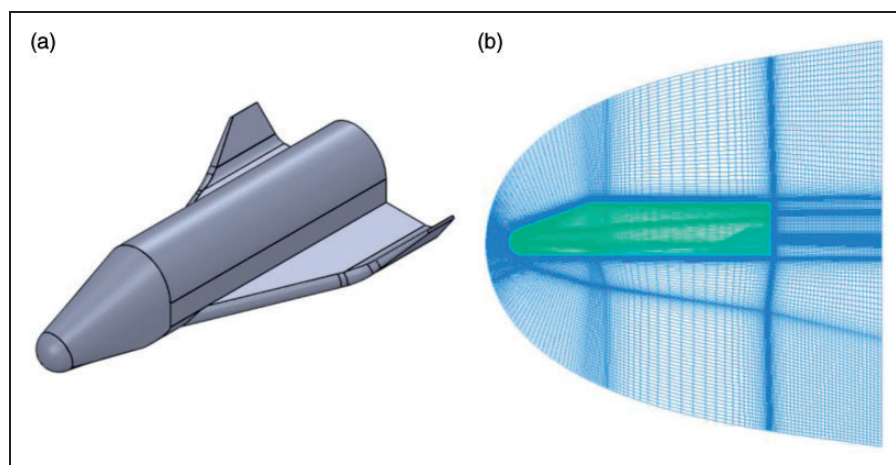


Figure 8. Geometric model of space shuttle and medium structured grid used for numerical simulations. (a) Geometric model and (b) medium structured grid.

structured grid employed in the space shuttle. To reduce the computational time, the medium grid scale is used for the following investigations for the space shuttle. Figure 8(b) shows the medium structured grid employed in the space shuttle.

In the numerical process, both the inviscid and viscous aerodynamic performances of the space shuttle for different angles of attack, ranging from -5° to 30° in increments of 5° , are obtained. The obtained inviscid and viscous results are compared with the experimental data,²⁶ as shown in Figure 9.

It is clear that the lift coefficients, lift-to-drag ratios, and pitching moment coefficients obtained from Euler code and SST $k-\omega$ turbulence model code are in good agreement with the experimental data²⁶ for the space shuttle in hypersonic flow conditions, see Figure 9(a), (c), and (d). When the angle of attack is no more than 15° , the drag coefficients obtained from the Euler code and SST $k-\omega$ turbulence model code closely match the experimental data. When the angle of attack is larger than 15° , the numerical drag coefficients obtained from the Euler code and SST $k-\omega$ turbulence model code are slightly overpredicted, see Figure 9(b).

Furthermore, the differences between the results obtained from the experiments and the numerical simulations seem small if only using the graphical comparison. To quantify the level of agreement between the computational results and experimental data, the relative errors (increment percentages) of the computational results relative to the experimental data are shown in Tables 6 and 7. As shown in Table 6, when the angle of attack is between -5° and 5° , the relative errors (increment percentages) of the computational results obtained from the SST $k-\omega$ turbulence model code relative to the experimental data are relatively large due to the fact that the absolute values of these parameters are quite small at the small angles of attack. And when the angle of attack is larger than 10° , the relative errors of the lift

coefficients, drag coefficients, pitching moment coefficients, and lift-to-drag ratios obtained from the SST $k-\omega$ turbulence model code relative to the experimental data are less than 13.4%, 18.3%, 8.0%, and 4.7%, respectively. As shown in Table 7, when the angle of attack is between -5° and 5° , the relative errors of the computational results obtained from the Euler code relative to the experimental data are relatively large due to the fact that the absolute values of these parameters are quite small at the small angles of attack. And when the angle of attack is larger than 10° , the relative errors of the lift coefficients, drag coefficients, pitching moment coefficients, and lift-to-drag ratios obtained from the Euler code relative to the experimental data are less than 16.3%, 12.3%, 6.6%, and 4.9%, respectively.

Moreover, as shown in Figure 9(b), the viscous and the Euler simulations are so close that the skin-friction drag seems to be negligible. There are two major reasons for that the skin-friction drag relative to the pressure drag is small in this space shuttle case. First, this is probably because the space shuttle is a comparatively blunt body so that the major source of the drag is the pressure drag due to the detached nose shock. This is consistent with the observations obtained by Zoby and Thompson.³⁰ Further, the pressure drag for some blunted bodies may account for nearly 100% of the total drag, as stated in Singh.³¹ Second, the viscosity coefficient of the free stream air is very small under the experimental setup in Li.²⁶ When given the free-stream Mach number (M_0) of 8.04, Reynolds number (Re_0) per unit of $1.13 \times 10^7/\text{m}$, total pressure ($P_{t,0}$) of 7.8 MPa, and total temperature ($T_{t,0}$) of 892 K, the free-stream static pressure (P_0) can be calculated by equation (8), i.e. 773.448 Pa, and the free-stream static temperature (T_0) can be calculated by equation (9), i.e. 64.042 K. And then, the viscosity coefficient (μ) of the free-stream air can be calculated from equation (10), i.e. $4.798 \times 10^{-6} \text{ kg}/(\text{m}\cdot\text{s})$. Thus, under the two

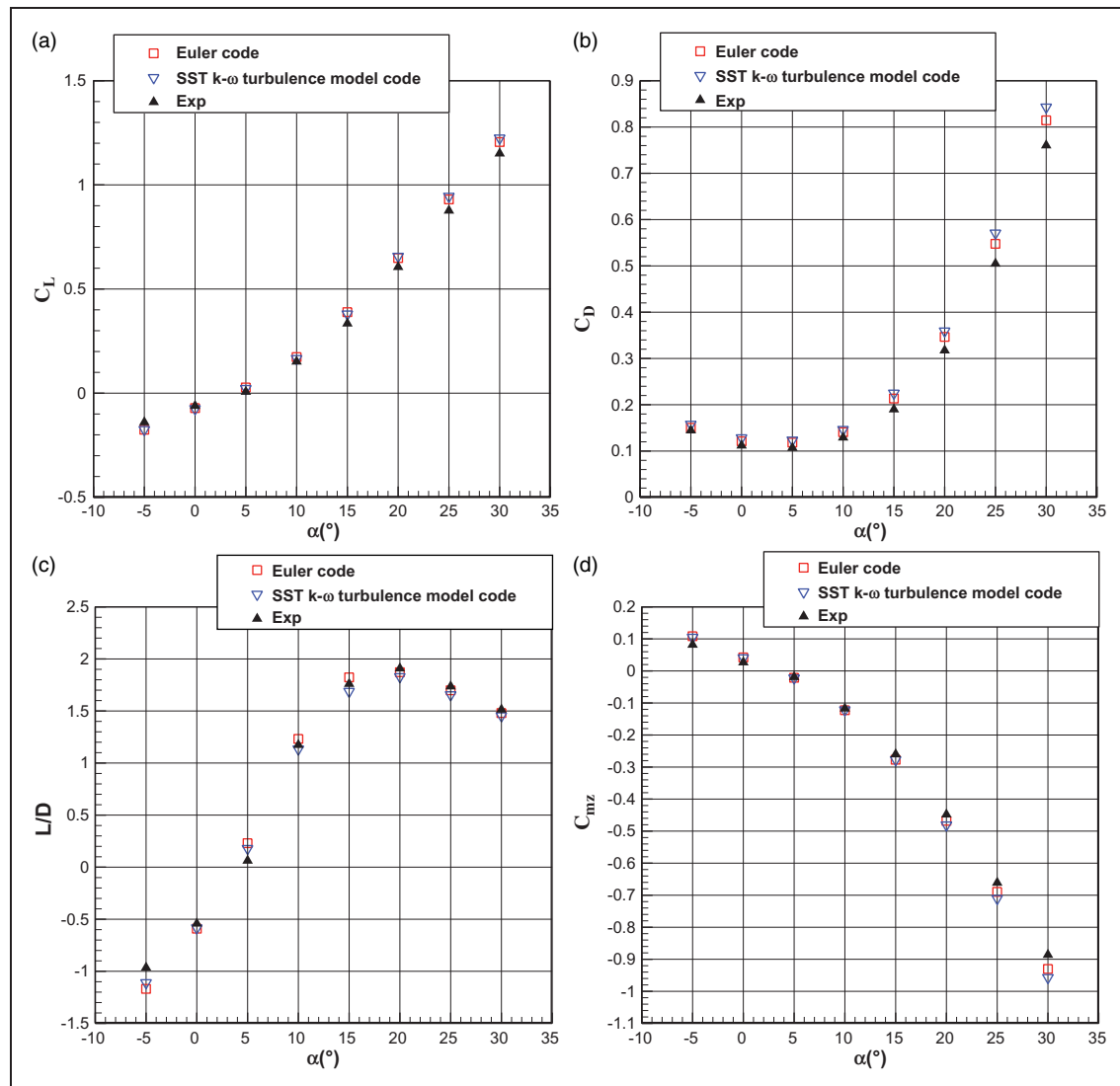


Figure 9. Comparison of aerodynamic performances of space shuttle (case I) as calculated using numerical computation and measured during the wind tunnel experiment. (a) Lift coefficient, (b) drag coefficient, (c) lift-to-drag ratio, and (d) pitching moment coefficient.

Table 6. Relative errors (increment percentages) of computational results obtained from SST $k-\omega$ turbulence model code relative to experimental data of space shuttle.

M_0	α (°)	ΔC_L	ΔC_D	ΔC_{Mz}	$\Delta L/D$
8.04	−5	25.3%	8.9%	27.8%	15.1%
8.04	0	23.7%	12.5%	51.0%	7.9%
8.04	5	229.0%	15.3%	16.8%	185.3%
8.04	10	9.2%	13.1%	4.2%	−3.4%
8.04	15	13.4%	18.3%	6.6%	−4.1%
8.04	20	8.4%	13.1%	7.4%	−4.2%
8.04	25	7.7%	13.0%	7.5%	−4.7%
8.04	30	6.4%	10.8%	8.0%	−4.0%

Table 7. Relative errors (increment percentages) of computational results obtained from Euler code relative to experimental data of space shuttle.

M_0	α (°)	ΔC_L	ΔC_D	ΔC_{Mz}	$\Delta L/D$
8.04	−5	25.7%	3.8%	32.3%	21.1%
8.04	0	18.0%	8.2%	56.3%	9.0%
8.04	5	307.4%	10.7%	11.6%	268.3%
8.04	10	14.3%	8.9%	4.7%	4.9%
8.04	15	16.3%	12.3%	6.6%	3.5%
8.04	20	7.1%	9.2%	4.4%	−1.9%
8.04	25	6.1%	8.5%	4.3%	−2.2%
8.04	30	4.8%	7.1%	5.0%	−2.2%

factors mentioned above, the skin-friction drag relative to the pressure drag is very small in this case.

$$\frac{P_{t,0}}{P_0} = \left(1 + \frac{\gamma-1}{2} M_0^2\right)^{\gamma/(\gamma-1)} \quad (8)$$

$$\frac{T_{t,0}}{T_0} = 1 + \frac{\gamma-1}{2} M_0^2 \quad (9)$$

$$\mu = \frac{P_0 M_0}{\text{Re}_0} \frac{\gamma}{\sqrt{(\gamma-1)C_p T_0}} \quad (10)$$

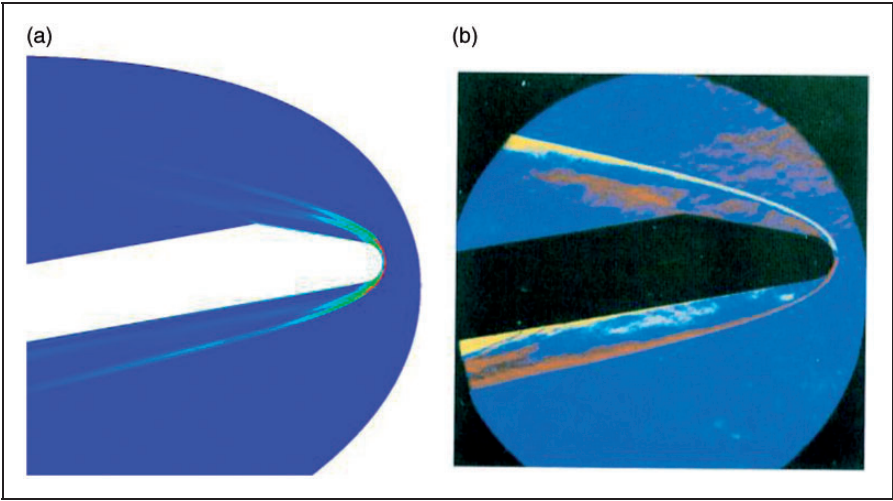


Figure 10. Comparison of experimental schlieren image and corresponding density gradient fields obtained from computation using the SST $k-\omega$ turbulence model employed in space shuttle. (a) CFD and (b) experiment.²⁶

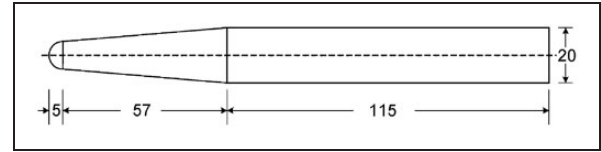


Figure 11. A sketch of the hypersonic slender vehicle (unit: mm).³²

Figure 10 shows a comparison of the experimental schlieren image and the corresponding density gradient fields obtained from the SST $k-\omega$ turbulence model code employed in the space shuttle case, when the angle of attack is 10° . It is obvious that the numerical results are in good agreement with the experimental data. The positions of the shock wave are almost the same.

Case 2. The experimental model of a hypersonic slender vehicle considered following the experimental work of Singh³¹ is the case 2 which is applied to further discuss the present code program, as done in our previous works.³² The experimental model consisted of three separate pieces: a hemispherical nose, a 5° half angle cone frustum, and a circular cylindrical section. The detailed dimensions of the experimental model can be seen in Figure 11.

The boundary conditions for the free stream are set as a Mach number of 8.2, a static pressure of 951.5 Pa, and a static temperature of 89.3 K, in accordance to the experimental setup in Singh.³¹ In the numerical process, the lift-to-drag ratios and pitching moment coefficients for different angles of attack, i.e. -3° , 0° , 3° , 5° , 7° , and 10° , are obtained, as done in Huang et al.³² Moreover, in this case, the length and base area (i.e. 17.7 cm and 3.14 cm^2) of the model are used as the reference length and area, respectively.

Table 8. Structured grid independency analysis employed in hypersonic slender vehicle (case 2) for SST $k-\omega$ turbulence model code ($M_0 = 8.2$, $\alpha = 10^\circ$).

	Number of cells	L/D	$\Delta L/D$
Coarse grid	779,483	1.137342	0.45%
Medium grid	941,463	1.136872	0.40%
Refined grid	1,103,443	1.132291	–

The reference point for the pitching moment is located at 5.2 cm from the model base.

In this study, three structured grid scales are introduced to analyze the grid independency. Table 8 presents the structured grid independency analysis obtained from the SST $k-\omega$ turbulence model code at the Mach number of 8.2 and the 10° angle of attack. In Table 8, the variation percentages of the lift-to-drag ratios for the coarse and medium grids are estimated relative to the refined grid.

Figure 12(a) and (b) presents the lift-to-drag ratios and pitching moment coefficients versus angle of attack, respectively. It is clear that the predicted lift-to-drag ratios and pitching moment coefficients show good agreement with the experimental data when the angle of attack is no more than 5° . When the angle of attack is larger than 7° , the numerical results are slightly underpredicted. Furthermore, although the Euler code solves the inviscid flow fields, the lift-to-drag ratios obtained from the Euler code are only slightly larger than those obtained from the SST $k-\omega$ turbulence model code, due to the fact that the skin-friction drag for the blunt body is relatively small in comparison to the pressure drag.³¹

From the earlier discussion, it can be concluded that the numerical method in this study can simulate the hypersonic vehicle within acceptable error

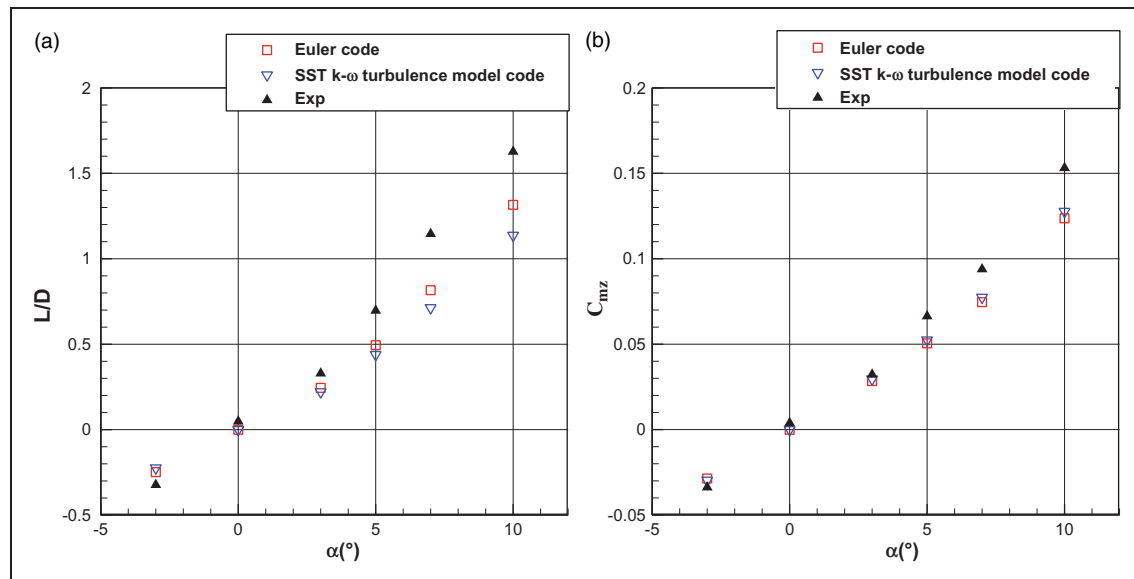


Figure 12. Comparison of aerodynamic performances of hypersonic slender vehicle (case 2) as calculated using numerical computation and measured during the wind tunnel experiment. (a) Lift-to-drag ratios and (b) pitching moment coefficient.

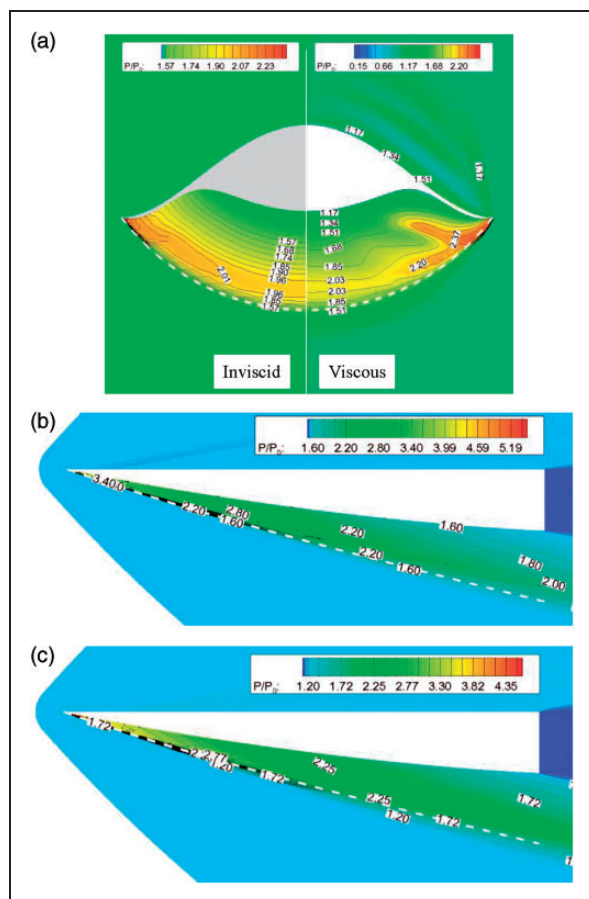


Figure 13. Comparison of inviscid and viscous nondimensional pressure contour lines at base and symmetric planes of von Karman waverider under design conditions: $H = 25$ km, $Ma = 6$, $\alpha = 0^\circ$. (a) Flow fields at the base plane, (b) inviscid flow field at the symmetric plane, and (c) viscous flow field at the symmetric plane.

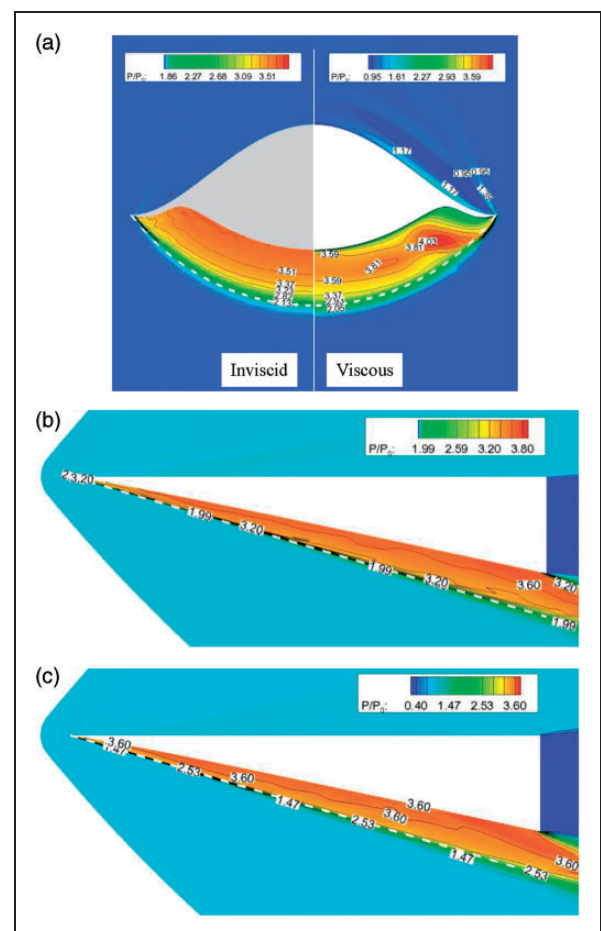


Figure 14. Comparison of inviscid and viscous nondimensional pressure contour lines at base and symmetric planes of cone-derived waverider under design conditions: $H = 25$ km, $Ma = 6$, $\alpha = 0^\circ$. (a) Flow fields at the base plane, (b) inviscid flow field at the symmetric plane, and (c) viscous flow field at the symmetric plane.

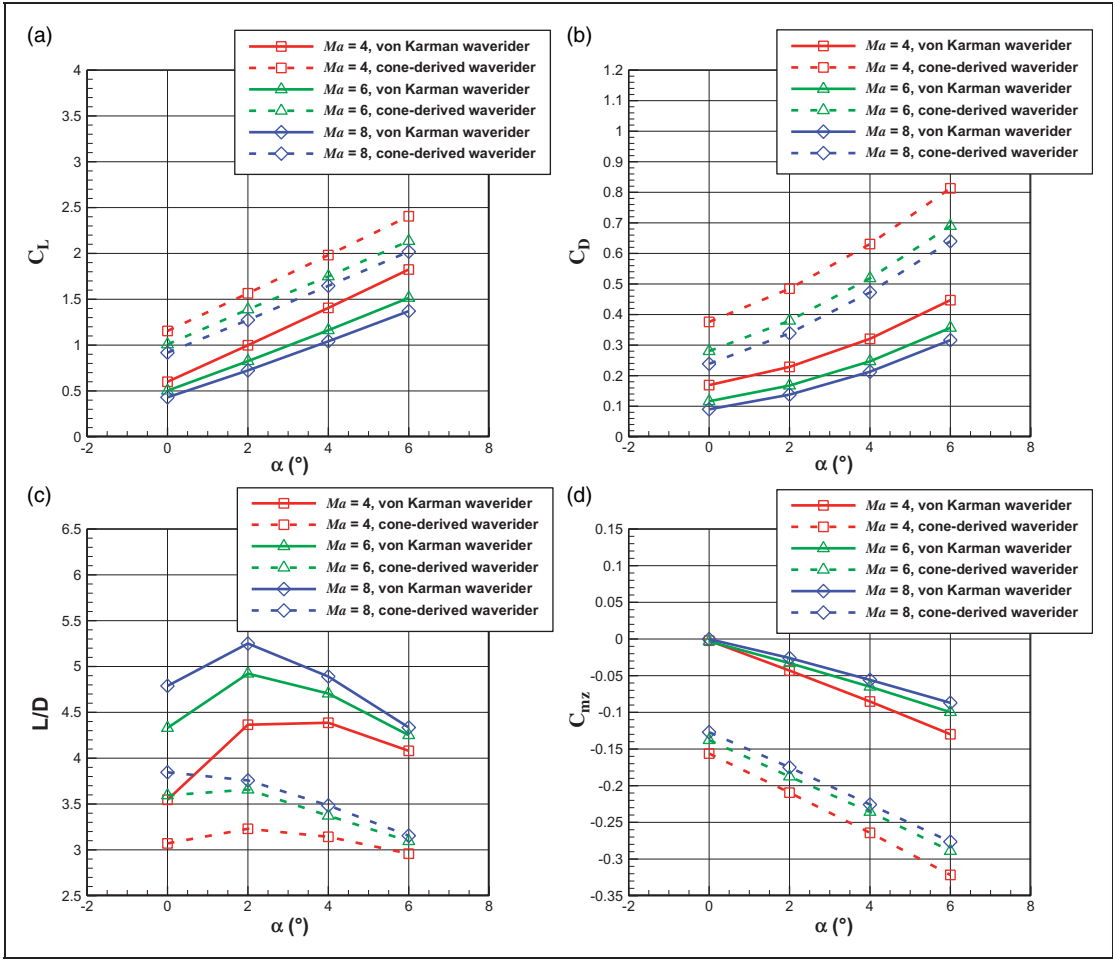


Figure 15. Comparison of viscous aerodynamic performances between cone-derived and von Karman waveriders. (a) Lift coefficient, (b) drag coefficient, (c) lift-to-drag ratio, and (d) pitching moment coefficient.

Table 9. Comparison of geometric parameters between cone-derived and von Karman waveriders.

	L_w (m)	W (m)	Vol (m ³)	S_{wet} (m ²)	S_b (m ²)	η
Cone-derived waverider	8.1102	4.8182	11.5508	50.8338	3.9247	0.1005
Von Karman waverider	8.6482	4.8182	9.1867	54.2601	2.2217	0.0808
Increment percentage	6.6%	—	−20.5%	6.7%	−43.4%	−19.6%

margins, and the numerical results are believable in the following parts.

Results and discussion

Verification of waverider generation

The inviscid and viscous nondimensional pressure contours at both the base planes and the symmetry planes of the two waveriders under the given design conditions are shown in Figures 13 and 14, respectively; these figures also give a comparison of the predicted and designed shock wave locations. The dashed lines in the figures represent the designed shock wave locations.

In the inviscid flow fields at the base and symmetric planes of the waveriders (Figures 13 and 14), the predicted shock wave locations by the numerical simulations show good agreement with the designed locations for the two waveriders. This validates the design procedure of the von Karman and cone-derived waveriders under the given design conditions for an inviscid flow.

As regards the viscous flow fields at the base plane of the waveriders (Figures 13 and 14), viscosity causes the high-pressure air between the compression-stream surface and the shock wave to leak to the free-stream surface. In the viscous flow fields at the base and symmetric planes of the waveriders (Figures 13 and 14), the shock wave locations obtained by the numerical

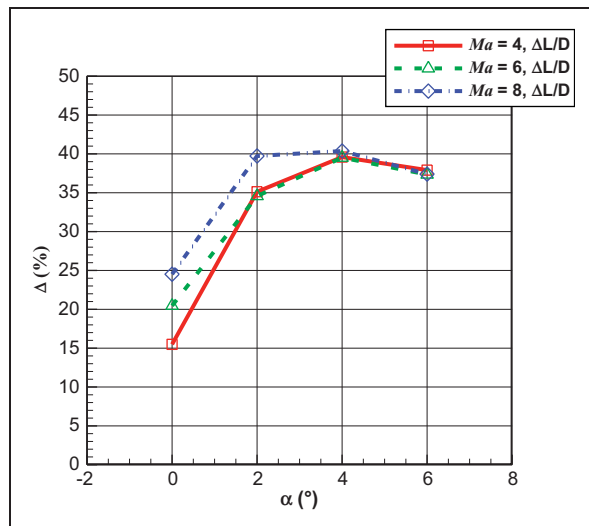


Figure 16. Increment percentage of lift-to-drag ratio of von Karman waverider relative to cone-derived waverider.

simulations are deflected downward from the designed locations, owing to the presence of the boundary layer.

Comparison of shapes and performances

Figures 4 and 15 show comparisons of the geometric models and the viscous aerodynamic performance, respectively, of the von Karman and cone-derived waveriders, while Table 9 presents a comparison of the geometric parameters between the von Karman and cone-derived waveriders. In Table 9, L_w and W are the length and width, respectively, of the waverider, while Vol is the internal volume, S_{wet} and S_b are the wet surface and base areas, respectively, and η is the volumetric efficiency, which is calculated from $Vol^{2/3}/S_{wet}$. From Table 9, the widths of the two waveriders are identical, because the trailing-edge curves of the free-stream surfaces are identical. The length and wet surface area of the von Karman waverider increase relative to those of the cone-derived waverider, while the internal volume, the base area, and the volumetric efficiency of the von Karman waverider decrease relative to those of the cone-derived waverider.

As shown in Figure 4(a) and (b), the von Karman waverider is much ‘thinner’ than the cone-derived waverider. And as shown in Figure 4(c), the von Karman waverider has a smaller cross section in the base plane than the cone-derived waverider. In addition, as can be seen in Figure 15(a) and (b), both the lift and the drag coefficients of the von Karman waverider decrease relative to those of the cone-derived waverider, owing to the 43.4% decrease in the base area of the former relative to that of the latter (see Table 9). Although the wet surface area of the von Karman waverider increases by 6.7% relative to that of the cone-

derived waverider (see Table 9), the viscous lift-to-drag ratios of the von Karman waverider increase relative to that of the cone-derived waverider under all the design and off-design conditions considered in the present study (see Figure 15(c)). Furthermore, as can be seen in Figure 15(d), the magnitude of the pitching moment of the von Karman waverider decreases relative to that of the cone-derived waverider. Because the decreased pitching moment can induce a reduction in the trim drag, the von Karman waverider has a smaller trim drag than the cone-derived waverider.

In order to analyze the variation in the lift-to-drag ratio in detail, the increment percentage of the lift-to-drag ratio of the von Karman waverider relative to that of the cone-derived waverider is determined, as shown in Figure 16. This figure clearly shows that the lift-to-drag ratio of the von Karman waverider increases by more than 35% relative to that of the cone-derived waverider when the angle of attack is larger than 2° .

Conclusions

In this study, a comparison between a novel waverider generated from an axisymmetric supersonic flow past a pointed von Karman ogive and a conventional cone-derived waverider generated from an axisymmetric supersonic flow past a cone was investigated. The novel waverider is termed a ‘von Karman waverider’. Numerical methods were employed to analyze the difference between the von Karman waverider and the conventional cone-derived waverider. From these investigations, we obtained the following conclusions:

- the von Karman waverider possesses lower drag and higher lift-to-drag ratios than the conventional cone-derived waverider;
- the conventional cone-derived waverider possesses higher internal volume and volumetric efficiency than the von Karman waverider; and
- the new basic flow field, namely the axisymmetric supersonic flow past the pointed von Karman ogive, will be very useful in the design of hypersonic waverider vehicles with lower drag and higher lift-to-drag ratios.

Acknowledgement

The authors are also grateful to the reviewers for their extremely constructive comments.

Conflict of interest

None declared.

Funding

The authors would like to express their gratitude for the financial support provided by the Fund of Innovation, Graduate School of NUDT (grant no. B140105) and the

Science Foundation of National University of Defense Technology (grant no. JC14-01-01).

References

- Liu J, Ding F, Huang W, et al. Novel approach for designing a hypersonic gliding-cruising dual waverider vehicle. *Acta Astronaut* 2014; 102: 81–88.
- Nonweiler TRF. Delta wings of shape amenable to exact shock wave theory. *J Royal Aeronaut Soc* 1963; 67: 39.
- Jones JG, Moore KC, Pike J, et al. A method for designing lifting configurations for high supersonic speeds, using axisymmetric flow fields. *Ingenieur-Archiv* 1968; 37: 56–72.
- Rasmussen ML. Waverider configurations derived from inclined circular and elliptic cones. *J Spacecraft Rocket* 1980; 17: 537–545.
- Corda S and Anderson JD. Viscous optimized hypersonic waveriders designed from axisymmetric flow fields. AIAA Paper 88-0369, 1988.
- Corda S. *Viscous optimized hypersonic waveriders designed from flows over cones and minimum drag bodies*. PhD Thesis, University of Maryland, Maryland, 1988.
- He XZ, Le JL and Wu YC. design of a curved cone derived waverider forebody. AIAA Paper 2009-7423, 2009.
- Mangin B, Benay R, Chanetz B, et al. Optimization of viscous waveriders derived from axisymmetric power-law blunt body flows. *J Spacecraft Rocket* 2006; 43: 990–998.
- Rodi PE. The osculating flowfield method of waverider geometry generation. AIAA Paper 2005-511, 2005.
- Goonko YP, Mazhul II and Markelov GN. Convergent-flow-derived waveriders. *J Aircraft* 2000; 37: 647–654.
- Mazhul II. Off-design regimes of flow past waveriders based on isentropic compression flows. *Fluid Dynam* 2010; 45: 271–280.
- Takashima N and Lewis MJ. Waverider configurations based on non-axisymmetric flow fields for engine-airframe integration. AIAA Paper 94-0380, 1994.
- Nielsen JN. *Missile aerodynamics*. New York: McGraw-Hill Book Co., Inc., 1960, pp.280–293.
- Zucrow MJ and Hoffman JD. *Gas Dynamics*. vol. 2. *Multidimensional flow*. New York: John Wiley and Sons, Inc., 1977, 112–266.
- Kothari AP, Tarpley C, McLaughlin TA. Hypersonic vehicle design using inward turning flow fields. AIAA Paper 96-2552, 1996.
- Liao JR, Isaac KM, Miles JB, et al. Navier–Stokes simulation for cone-derived waverider. *AIAA J* 1992; 30: 1521–1528.
- ANSYS. *ANSYS FLUENT Theory Guide*. Release 13.0. Canonsburg, PA: ANSYS, Inc., 2010.
- Huang W, Wang ZG, Ingham DB, et al. Design exploration for a single expansion ramp nozzle (SERN) using data mining. *Acta Astronaut* 2013; 83: 10–17.
- Huang W, Wang ZG, Pourkashanian M, et al. Numerical investigation on the shock wave transition in a three-dimensional scramjet isolator. *Acta Astronaut* 2011; 68: 1669–1675.
- Huang W and Wang ZG. Numerical study of attack angle characteristics for integrated hypersonic vehicle. *Appl Math Mech* 2009; 30: 779–786.
- Huang W, Liu WD, Li SB, et al. Wang, Influences of the turbulence model and the slot width on the transverse slot injection flow field in supersonic flows. *Acta Astronaut* 2012; 73: 1–9.
- Mansour K and Khorsandi M. The drag reduction in spherical spiked blunt body. *Acta Astronaut* 2014; 99: 92–98.
- Chen XQ, Hou ZX, Liu JX, et al. Bluntness impact on performance of waverider. *Comput Fluid* 2011; 48: 30–43.
- Liu JX, Hou ZX, Chen XQ, et al. Experimental and numerical study on the aero-heating characteristics of blunted waverider. *Appl Thermal Eng* 2013; 51: 301–314.
- Roy CJ and Blottner FG. Review and assessment of turbulence models for hypersonic flows. *Progr Aerosp Sci* 2006; 42: 469–530.
- Li SX. *The flow characteristics for the typical model in hypersonic flows*. Beijing, China: National Defence Industry Press (in Chinese), 2007, pp.15, 181–185.
- Ding F, Shen C-B, Liu J, et al. Influence of surface pressure distribution of basic flow field on shape and performance of waverider. *Acta Astronaut* 2015; 108: 62–78.
- Liu JX, Hou ZX, Ding GH, et al. Numerical and experimental study on waverider with blunt leading edge. *Comput Fluid* 2013; 84: 203–217.
- Anderson JD. *Hypersonic and high temperature gas dynamics*. 2nd ed. Virginia: AIAA, Inc., 2006, p.459.
- Zoby EV and Thompson RA. Flowfield and vehicle parameter influence on hypersonic heat transfer and drag. *J Spacecraft Rocket* 1990; 27: 361–368.
- Singh A. *Experimental study of slender vehicles at hypersonic speeds*. PhD Thesis: Cranfield University, Cranfield, 1996.
- Huang W, Li SB, Liu J, et al. Investigation on high angle of attack characteristics of hypersonic space vehicle. *Sci China Technol Sci* 2012; 55: 1437–1442.

Appendix I

Notation

C_D	drag coefficient
C_L	lift coefficient
C_{mz}	pitching moment coefficient
C_p	specific heat at constant pressure, J/(kg.K)
k	thermal conductivity of gas, W/(m.K)
L	length of von Karman ogive, m
L/D	lift-to-drag ratio
L_w	length of waverider, m
R	base radius of von Karman ogive, m
Ma	flight Mach number
M_0	free-stream Mach number
P_0	free-stream pressure, Pa
P	local static pressure, N/m ²
P/P_0	ratio of local to free-stream static pressures

Pr	Prandtl number	Vol	internal volume of waverider, m^3
$P_{t,0}$	free-stream total pressure, Pa	W	width of waverider, m
Re_0	free-stream Reynolds number per unit, /m	y	distance to the nearest wall, m
R_S	radius of shock wave at the base plane, m	y^+	dimensionless distance from the wall
S_b	base area of waverider, m^2	α	angle of attack, $^\circ$
S_{wet}	wetted surface area of waverider, m^2	η	volumetric efficiency
T_0	free-stream temperature, K	θ_A	angle of slope at point A , $^\circ$
$T_{t,0}$	free-stream total temperature, K	μ	dynamic viscosity coefficient, $kg/(m.s)$
u_τ	friction velocity at the nearest wall, m/s	ν	kinematic viscosity coefficient, m^2/s